ASTM D5946
ASTM D7334
ASTM D7490
ISO 27448

optical contact angle measurements and drop contour analysis to determine surface energy as well as interfacial and surface tension

force tensiometry, dynamic contact angle measurements, and force of adhesion evaluation

ASTM D1331
ASTM D1417
ISO 1409

ISO/TR 13097

optical turbidity, stability and aging analysis of multi-phase dispersions

zeta potential measurements of fibres, powders, and plate-shaped solids

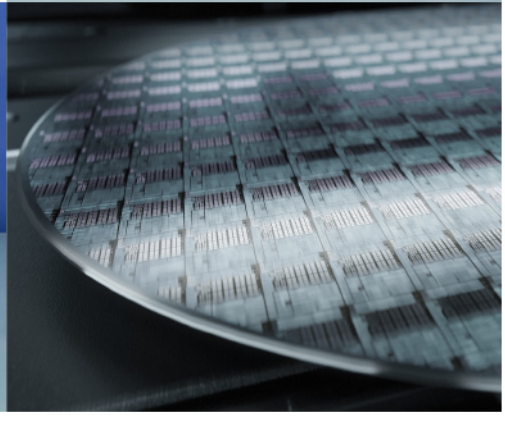

High-end, versatile laboratory measurement device portfolio for a comprehensive analysis of surfaces and interfaces

Learn more >

dataphysics
Understanding Interfaces

DataPhysics Instruments GmbH
Raiffeisenstraße 34 • 70794 Filderstadt, Germany
phone +49 (0)711 770556-0 • fax +49 (0)711 770556-99
sales@dataphysics-instruments.com
www.dataphysics-instruments.com

ADVANCED FUNCTIONAL MATERIALS
www.afm-journal.de

Calibration-Free and High-Sensitivity Microwave Detectors Based on InAs/InP Nanowire Double Quantum Dots

Samuele Cornia, Valeria Demontis, Valentina Zannier, Lucia Sorba, Alberto Ghirri, Francesco Rossella,* and Marco Affronte*

At the cutting-edge of microwave detection technology, novel approaches which exploit the interaction between microwaves and quantum devices are rising. In this study, microwaves are efficiently detected exploiting the unique transport features of InAs/InP nanowire double quantum dot-based devices, suitably configured to allow the precise and calibration-free measurement of the local field. Prototypical nanoscale detectors are operated both at zero and finite source-drain bias, addressing and rationalizing the microwave impact on the charge stability diagram. The detector performance is addressed by measuring its responsivity, quantum efficiency and noise equivalent power that, upon impedance matching optimization, are estimated to reach values up to ≈2000 A W^{-1}, 0.04 and ≈10^{-16} W / $\sqrt{Hz}$, respectively. The interaction mechanism between the microwave field and the quantum confined energy levels of the double quantum dots is unveiled and it is shown that these semiconductor nanostructures allow the direct assessment of the local intensity of the microwave field without the need for any calibration tool. Thus, the reported nanoscale devices based on III-V nanowire heterostructures represent a novel class of calibration-free and highly sensitive probes of microwave radiation, with nanometer-scale spatial resolution, that may foster the development of novel high-performance microwave circuitries.

1. Introduction

Microwave (MW) radiation plays a key role in countless applications ranging from information and communications technologies to medical diagnostics,[1] and represents an important tool for the development of quantum science and technology by enabling the manipulation and readout of qubits encoded in solid state platforms.[2–5] Moreover, innovative MW detectors may open exciting perspectives in astrophysics,[6] for instance, fostering novel approaches to the probing of the cosmic background radiation and the search for dark matter particles.[7] In general, compared to optical radiation, the detection of microwave photons is quite challenging, mainly due to the small energy scale involved. In fact, for radiation frequencies in the 1–300 GHz range, equivalent photon energies range from few μeV to about 1 meV. The detection of photons of such small energy requires detectors operated at ultra low temperatures, to suppress the thermal background, and several precautions have to be taken into account in order to preserve the system from phonon coupling and any other source of noise. While several systems and methods have been proposed for the detection of MW radiation in different regimes,[8] still no universal approach is available. Conversely, the materials, architectures and active mechanisms exploited in MW detectors may strongly depend on the targeted application. Microwave detectors based on Josephson junction devices were reported in the 4–20 GHz range.[3] In the same range, opto-electromechanical detectors have also been theoretically proposed, while different types of superconductive bolometers have been operated in the frequency range above 300 GHz, with promising potential extensions at frequencies down to 90 GHz.

S. Cornia
Dipartimento di Scienze Fisiche Informatiche e Matematiche
Università di Modena e Reggio Emilia
via G. Campi 213/A, 41125 Modena, Italy
E-mail: samuele.cornia@unimore.it
S. Cornia
Dipartimento di Fisica
Università di Pavia
via A. Bassi 6, 27100 Pavia, Italy
The ORCID identification number(s) for the author(s) of this article can be found under https://doi.org/10.1002/adfm.202212517.

DOI: 10.1002/adfm.202212517

V. Demontis, V. Zannier, L. Sorba
Istituto Nanoscienze
Consiglio Nazionale delle Ricerche
Piazza San Silvestro 12, 56127 Pisa, Italy
V. Demontis, V. Zannier, L. Sorba, F. Rossella, M. Affronte
NEST
Scuola Normale Superiore
Piazza San Silvestro 12, 56127 Pisa, Italy
E-mail: francesco.rossella@sns.it
A. Ghirri, M. Affronte
Istituto Nanoscienze
Consiglio Nazionale delle Ricerche
via G. Campi 213/A, 41125 Modena, Italy

In recent years novel architectures based on semiconductor nanowires (NWs) have been proposed for the manipulation[9] and detection of high frequency radiation. These include arrays of NW diodes[10] and NW field effect transistors[11] for probing THz radiation,[12,13] as well as NW quantum dot (QD) systems coupled to superconducting resonators.[14–16] NW QDs - can be realized electrostatically using gate electrodes[17–20] to control tunnel barriers and chemical potentials in the dots, resulting in zero dimensional systems with relatively large dot size and weak confinement owing to the small energy distance among quantum confined energy levels. These systems can be relatively easily exploited for MW emission[21,22] and detection down to single photons.[23–25] On the other hand, hard-wall NW QD systems—both single and multiple NW QDs—can be realized exploiting the InAs/InP NW heterostructure technology, which allows to grow few nm-thick InP barriers inside an InAs NW, that may induce quantum confinement along the NW axis.[26] This technology allows to engineer NW QDs-based devices displaying extremely large charging energy as well as quantum confined energy, both exceeding 10 meV at 4.2 K.[27–29] In the case of InAs/InP NW double quantum dots (DQDs), such energetics may coexist with the onset of clean Pauli spin blockade up to 10 K.[30] Overall, these unique features make InAs/InP NW DQD systems impressively resilient to temperature and magnetic field.[31] In addition to the large energy scales and the robust current blockade features , InAs/InP NW DQD are also highly tunable by external gate potentials. This allows, in principle, the continuous tuning of energy levels spacing from GHz to THz frequencies. While these features overall suggest that InAs/InP NW DQD based devices may offer intriguing perspectives for the detection of MW radiation, their full exploitation as MW detectors still represents an open challenge.

In this work, we exploit hard wall InAs/InP NWs to address the impact of a MW field on the transport properties of electrons tunneling across a semiconductor DQD. MW radiation in the range 1–10 GHz was applied to NW DQD-based devices equipped with source and drain electrodes and two independently biased side gates, inducing quantitative and qualitative changes in the charge stability diagram of the nanodevices. Focusing on the triple points, at vanishing source-drain bias, V_{DS}, we map the evolution of the charge stability diagram as function of the MW input power and we address the responsivity of our devices, carefully ruling out the effect of temperature broadening. At finite V_{DS}, the characteristic current triangles emerging in the stability diagram widen in both the filling and detuning directions upon the application of MWs, while current spots with sign opposite to V_{DS} emerge exactly in correspondence of the zero-bias triple points. To rationalize our experimental outcomes both at zero and finite V_{DS} and explore the mechanism of interaction of the MW field with the NW-based device, we resorted to a phenomenological model, which invokes an effective alternating current (AC) bias to account for the MW field's coupling with the NW-DQD. This bias has the effect of shaking the chemical potentials in the leads, which in turn affects the addition energies in the dots via lead-dot capacitive coupling, inducing a shift in the relative alignment of the potentials in the leads and the dots, due to the MWs. Overall, this explains the main features observed in the charge stability diagrams and allows us to address the local amplitude of the AC drive at the device without resorting to power calibrations.

We quantify the performance of our NW-DQD based MW detectors with three figures of merit, namely the responsivity, R, the quantum efficiency, η, and the noise equivalent power, NEP. We found that upon optimal MW-detector coupling our devices display surprisingly high R and η (up to 2000 A W^{-1} and 0.04, respectively) and low NEP (down to $10^{-16}\,W/\sqrt{Hz}$). Our work suggests that the unique combination of transport features and subwavelength dimensions offered by InAs/InP NW DQDs make these nanomaterials potential game changers for future MW detection platforms and applications.

2. Results and Discussion

2.1. Device Architecture and Operation

Figure 1a reports the false color scanning electron micrograph of one of the measured InAs/InP NW DQD-based devices, equipped with source (S) and drain (D) electrodes (blue colored) and two side gates (G1-2, green colored). We measured 7 devices, fabricated starting from the same NW batch, and we carried out 8 measurement campaigns in the temperature range 2–8 K. Nanodevices are fabricated by depositing the nanowires onto a Si++/SiO_2 substrate that can be used as a backgate. This can be used in combination with two side gates allowing to fully configure and control the direct current (DC) transport features—the stability diagram—of the InAs/InP DQD. The inset shows the scanning electron micrograph of the InAs NW region embedding the three InP barriers (nominal thickness 5 nm) which separate two asymmetric InAs sections (nominal thicknesses 20 nm and 23 nm) defining the DQD (see also the Methods section). Figure 1b reports the schematic of the experimental setup—the measurement circuit—together with the nanodevice equivalent circuit (inset). S-D DC bias voltage application and S-D current readout were performed with a source-measure unit, the gates were voltage-biased by stabilized DC sources and MWs were applied resorting to a radio frequency (RF) line, bonded to one of the chip pads at a distance of ≈2 mm from the nanodevice. In Figure 1(b-inset), quantum dots labeled 1 and 2 are connected in series and coupled to source and drain leads via tunneling barriers characterized by resistive and capacitive components and are also capacitively coupled to external gate voltages (only side gates indicated).[32] The device control scheme envisions three gates (one back and two sides) acting on the whole DQD (global gates)[30] rather than local gates acting separately on each QD.[33] Device current response is measured as a function of effective side gate voltages V'_{G1} and V'_{G2} corresponding to linear combinations of the voltages V_{G1} and V_{G2} physically applied to side gates G1 and G2, according to $V'_{G1} = \frac{1}{\sqrt{2}}(V_{G2} - V_{G1})$ and $V'_{G2} = \frac{1}{\sqrt{2}}(V_{G1} + V_{G2})$ (Section 1, Supporting Information). The control over the DQD filling stems from the average component of the electric field, proportional to V'_{G2} (balanced gate voltage configuration), whereas the the DQD detuning is controlled by the transverse or Stark component of the electric field, proportional to V'_{G1} (unbalanced gate voltage configuration). This kind of control

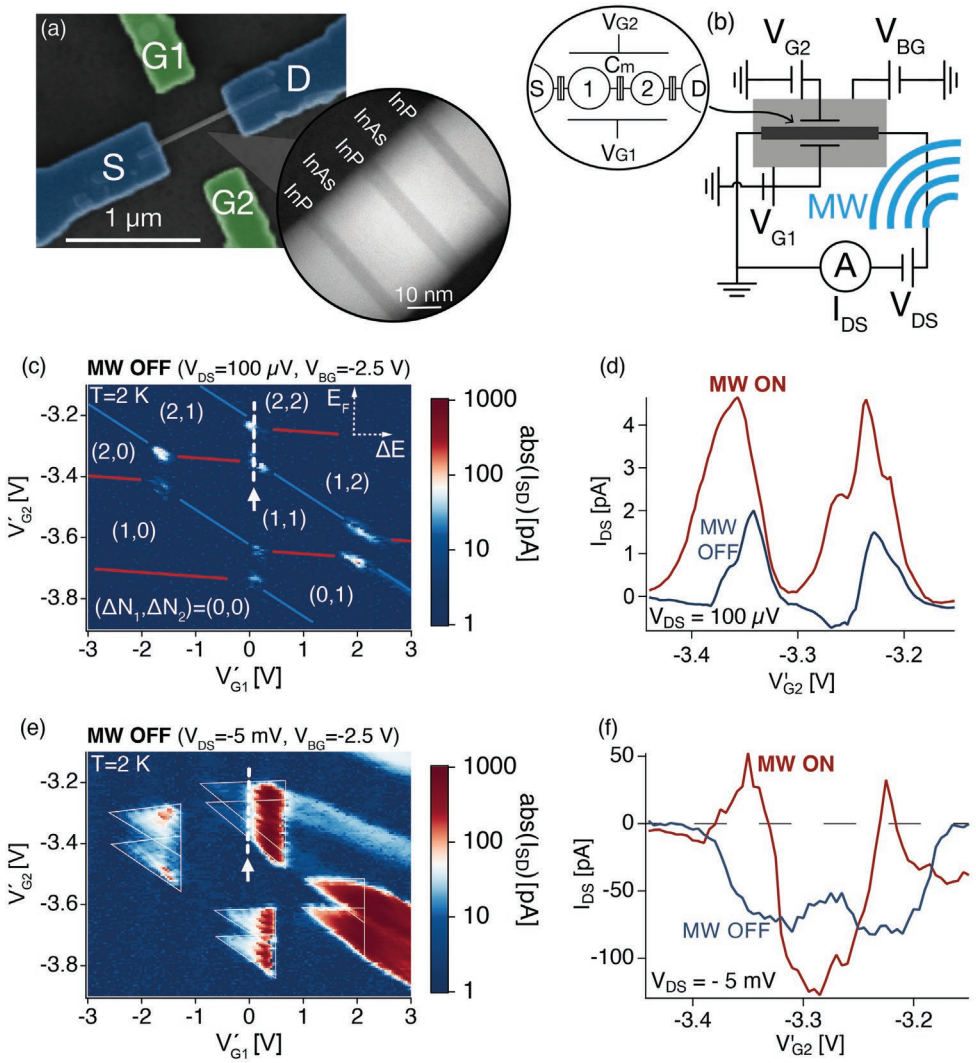

Figure 1. a) Scanning electron micrograph of one of the measured devices, comprising of source (S) and drain (D) contacts and gate electrodes (G1,G2). Inset: Scanning tunneling electron micrograph of an InAs/InP nanowire double quantum dot (NW-DQD)measured in this work. b) Pictorial view of the experimental setup. A source-measure unit (not shown) is used to voltage bias (V_{DS}) the nanodevice and measure the current intensity (I_{DS}). Microwaves are fed through an external antenna. Inset: model of the DQD system. The two QDs are represented by conductive islands connected in series and connected to source and drain contacts through tunneling barriers. Two side gates and a backgate (not represented in the model) control the DQD filling and provide a transverse electrostatic field to achieve detuning by exploiting the quantum confined Stark effect. c) Stability diagram of the NW-DQD measured at T = 2 K and $V_{BG} = -2.5$ V, without MW applied at vanishing V_{DS}, with triple points marking the edges of regions with fixed occupation number, labeled with (ΔN_1, ΔN_2). $\Delta N_{1(2)}$ marks the number of additional electrons present in QD 1(2) with respect to a reference point. d) Current trace at zero V_{DS} measured along the white dotted line evidenced in panel (c) (filling direction across two triple points) with (red curve) and without (blue curve) MW excitation. e) Stability diagram without MW applied measured at $V_{DS} = -5$ mV; characteristic current triangles marked by white contour. f) Current trace at $V_{DS} = -5$ mV measured along the white dotted line evidenced in panel (e) with (red curve) and without (blue curve) MW excitation.

exploits the quantum-confined Stark effect and it is possible thanks to the asymmetry of the system, provided by the slight differences between the axial lengths of the two dots and their occupied electron orbitals.

Figures 1c and 1e report the device stability diagrams (color-plots of I_{DS} as a function of V'_{G1} and V'_{G2}) measured at 2 K, $V_{BG} = -2.5$ V and at zero MW power, for vanishing (1c) and finite (1e) S-D bias voltage applied. At $V_{DS} = 0$ V (Figure 1c), transport is permitted only when the chemical potentials of S and D leads are aligned to the QD addition energies: this configuration corresponds to the white-colored point-like current spots arranged in a honeycomb fashion in Figure 1c. In the top-right corner of the current map, the dashed axes labeled E_F and ΔE indicate the filling and detuning directions of the DQD, respectively. Along the filling direction, the total number of electrons confined in the DQD increases together with the electron population of each dot. Along the detuning direction, the number of electrons confined in the DQD remains constant while electrons redistribute in the two QDs. According to the electron population in the left and right dot (or dot 1 and 2 in Figure 1(b-inset), different regions of the charge stability diagram are labeled (i, j) with i and j being the number of electrons

inside dot 1 and 2, respectively. Consistently, the locations of the current spots are referred to as triple points, connecting three regions of the stability diagram with different electron population, such as for instance the regions (1,1), (2,0) and (2,1). At finite V_{DS} (Figure 1e) for each triple point a finite energy window opens in which transport is allowed and a current triangle is observed in the stability diagram. From the analysis of the two datasets and resorting to the DQD model schematically shown in the inset of Figure 1b, all physical parameters identifying the DQD can be extracted[32] including the charging and electrostatic coupling energies (≈10 meV), the gate lever arms (≈20 meV V^{-1}), the dot capacitances (≈20 aF) (see Section 2, Supporting Information).

2.2. MW Impact on Current Traces at Triple Points

Figure 1d reports current traces measured along the filling direction (V'_{G2} axis) in the zero-bias stability diagram (white dashed segment in panel (c)) with (red curve) or without (blue curve) MW applied to the device. The two peaks, corresponding to the two triple points connecting clock-wise the regions (1,1), (2,1), (2,2) and (1,2), display marked amplification (current intensity increase) as well as broadening upon application of the MW field. Figure 1f highlights the effect of the MWs over the current profile connecting along the filling direction a pair of current triangles measured at finite bias ($V_{DS} = -5$ mV). The MW-OFF current trace (blue curve) is robust (order of 100 pA), always negative (according to the bias sign) and displays a faint symmetric trend with respect to $V'_{G2} = -3.3$ V. With MW turned ON, the current profile (red curve) maintains its symmetry with respect to $V'_{G2} = -3.3$ V, however, it exhibits a reversal of the derivative with respect to the blue curve and the emergence of two peaks of positive current. In the following we shall investigate in detail the MW response of NW-DQD devices in both zero and finite bias configurations as function of effective gate voltages and MW nominal power, ruling out thermal effects and providing a phenomenological model to rationalize the observed results.

2.3. Probing MWs at Zero V_{DS}

Figure 2 illustrates the effect of the MW field on the NW-DQD charge stability diagram at zero V_{DS} ($V_{BG} = -2$ V, T=2 K), tuning V'_{G1} and V'_{G2} in the proximity of a pair of triple points. In absence of a MW field, the triple points appear as reported in Figure 2a. Here, the red segment identifies the detuning direction corresponding to the scanning of the effective gate voltage $V_G^* = 0.76 \times V_{G1} - 0.65 \times V_{G2}$ in the range 2.66–2.80 V. Figure 2b

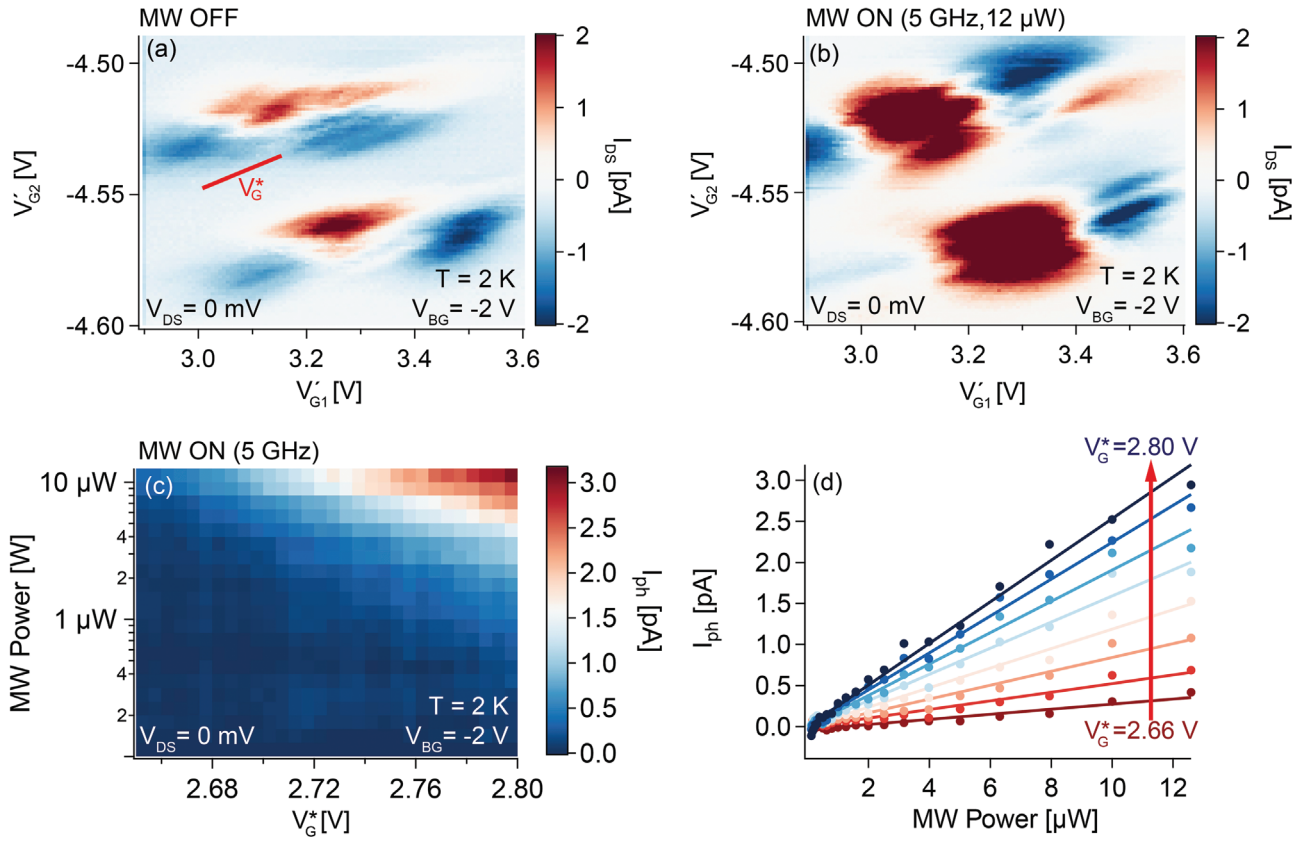

Figure 2. Current triple points measured at vanishing bias (T=2 K, $V_{DS} = 0$ mV, $V_{BG} = -2$ V): a) without MW excitation and b) upon MW input power of 12 μW. The red segment indicates the detuning direction, which corresponds to the scanning of the effective gate voltage V_G^* (defined in the main text). c) Photocurrent map as function of V_G^* and MW power, at fixed frequency. d) Vertical cuts of the current map reported in (c), that is, photocurrent curves as function of MW power for different values of V_G^*. Linear fitting curves are reported and used to estimate the responsivity R.

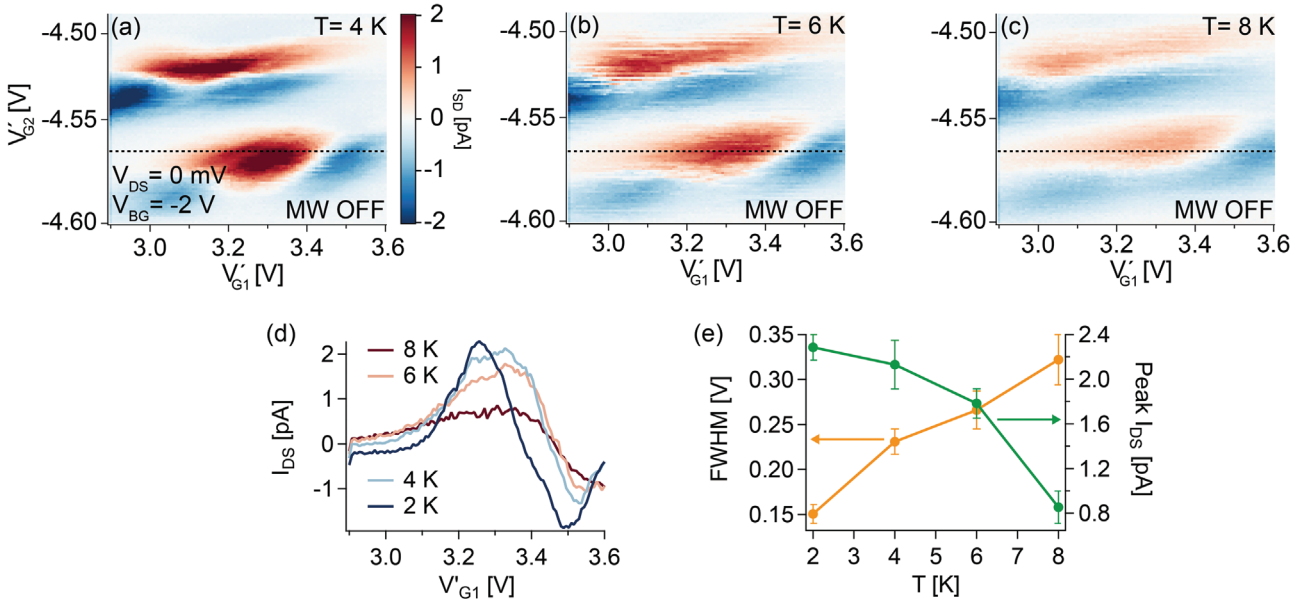

Figure 3. Current maps at triple points measured at zero MW power at temperatures T=4 K (a), T=6 K (b) and T=8 K (c). (The map at T=2 K is reported in Figure 2a). The effect of temperature on the stability diagram differs abruptly from the effect of the MW shown in Figure 2b. d) Current traces measured along the dotted line in (a) at different temperatures. e) Full width at half maximum (FWHM) and positive current peak intensity extracted from (d).

reports the charge stability diagram measured upon the application of MWs with frequency of 5 GHz and power of 12 μW: the triple points are emphasized by the MWs, with an overall increase of the current level and a widening of each triple point along both filling and detuning directions. We note that all MW power values reported take into account the measured attenuation along the RF lines (see Section 8, Supporting Information). Figure 2c shows the photo-current (I_{ph}) map measured by scanning V_G^*, for different values of the applied MW power in the range from 100 nW to 12 μW. The current increases markedly from the bottom-left corner of the colorplot to the top-right corner. Figure 2d reports I_{ph} as a function of the MW power, for different values of V_G^*. Each dataset (set of points with fixed color) corresponds to a vertical cut of the map in Figure 2c. All the measured I_{ph} traces reported in Figure 2d are linearly proportional to the MW power, as evidenced by the solid curves that correspond to linear fits of the experimental points: this indicates that NW-DQD devices may operate as power law MW detectors.

The response of the NW-DQD-based devices as MW detector can be quantified extracting the responsivity R, a key figure of merit which measures the intensity of the output signal for a given input power. R can be extracted as the slope of the linear fit of I_{ph} as function of the MW power (Figure 2d). An alternative way to quantify the detector response consists in reporting the quantum efficiency $\eta = \frac{n_e}{n_{hv}}$, which measures the photon-to-charge conversion as the number of photoelectrons generated for each impinging MW photon. η can be directly derived from the responsivity, as reported in Section 4.2, Supporting Information. The maximum responsivity of our devices is obtained at zero detuning and corresponds to the slope of the blue line measured at $V_G^* = 2.80$ V in Figure 2d. This slope was found to provide $R = 250 \pm 10$ nA W^{-1}, which in turn implies $\eta \approx 10^{-12}$. We also extracted the noise equivalent power (NEP) of our devices, that is, the input power for which a signal-to-noise ratio of 1 is obtained in a 1 Hz measurement bandwidth.[34] The lowest NEP is obtained at maximum responsivity and was found to be $NEP = 1.2\,\mu W / \sqrt{Hz}$ (Section 4.3, Supporting Information).

It is worth noting that the values reported above for maximum R and η (and minimum NEP) represent lower bounds to the actual performance of our NW-DQD MW detectors, because these values (i) do not take into account the MW power losses due to the antenna-detector coupling and (ii) assume unitary absorption of the MW radiation in the NW cross-section. Regarding point (i), we estimate the power losses by considering the radiated power at the antenna and by assuming irradiation with cylindrical symmetry, and this bring us to define an antenna-detector losses renormalization factor, L_{AD} (details in Section 4.4, Supporting Information). We estimated $L_{AD} \approx 3.5 \times {}^{-5}$ for the MW power impinging onto the NW detector, yielding to renormalized values for maximum R and η and for minimum NEP, namely 7 mA W^{-1}, 5×10^{-7} and $40 pW / \sqrt{Hz}$, respectively. Regarding point (ii), as will be clarified in the following section, we estimate the effective MW absorption in the NW cross-section by resorting to finite-bias spectroscopy measurements.

The entire study reported above, carried out at a MW frequency of 5 GHz, was repeated at different frequencies without observing any significant difference, except for the expected frequency dependent attenuation of the experimental setup (Section 7, Supporting Information). Importantly, the occurrence of transport features substantially unaffected by the change of the MW energy suggests that we can exclude photon assisted tunneling from the possible mechanisms of interaction between the DQD and the MW.[35,36] Moreover, the features observed in the current maps upon the application of a MW field are not ascribable to trivial heating effects potentially associated

to the impact of the MWs. This was ascertained by addressing the effect of temperature on the stability diagram at MW OFF and measuring the same pair of triple points at four different temperatures in the range 2–8 K, as reported in Figure 2a and **Figure 3**a–c. Figure 3d reports the current profiles measured along the black dashed line shown in Figure 3a at T = 2 K, 4 K, 6 K and 8 K. For each curve, from the current peak observed at gate voltage of about 3.3 V, we extracted the full width at half maximum (FWHM) and the intensity. The results of this analysis, reported in Figure 3e, clearly indicate that a temperature increase induces an overall broadening of the current features accompanied by a drastic decrease of the current intensity: this is absolutely not consistent with the observed strong increase of the current level due to the application of MWs, as reported in Figure 2b. In addition, we also exclude thermoelectric effects or phonon assisted transport phenomena due to asymmetric heating at the leads, that may establish a temperature gradient. Indeed, such effects are associated to the occurrence of very unique transport features in the stability diagram, such as triangularly shaped current side bands with sign reversal,[37,38] that were never observed in our experiments.

2.4. Probing MWs at Finite V_{DS}

The high figure of merit envisioned in InAs/InP NW-DQDs coexists with the possibility to operate the nanodevices as calibration-free or absolute MW detectors. This stems from the peculiar transport characteristics displayed by DQDs at finite V_{DS}. **Figure 4**a reports two pairs of current triangles measured at $V_{DS} = -5$ mV and MW-OFF ($V_{BG} = -2.5$ V, T=2 K). The current is significantly quenched at the base of the left triangles with respect to the right ones, consistently with a Pauli spin blockaded transport in the left triangle pair. Figure 4b reports the charge stability diagram measured upon the application of MWs with frequency of 1.2 GHz and power of 100 μW. Overall, the impact of the MWs is two-fold: the magnification of the size of each current triangle, together with the rise of two current spots with sign reversal with respect to the main triangle (positive current spots inside negative current triangles).

Regarding the triangle magnification effect, we notice that in DC bias spectroscopy experiments the widening of triangles is proportional to the increase of V_{DS} and corresponds to an increased range of energetic configurations fitting inside the bias window.[32] This bring us to introduce an effective bias V_{DS}^{eff} accounting for the triangle magnification due to the MWs. With the energetics of the NW-DQD known from the finite bias spectroscopy at zero power MWs (Sections 1 and 2, Supporting Information), we estimate that the increased triangle size reported in Figure 4b corresponds to $V_{DS}^{eff} = -10 \pm 1$ mV. This is confirmed by a direct comparison of the MW-ON stability diagram with the $V_{DS} = -10$ mV, MW-OFF stability diagram (Section 6, Supporting Information). The four current spots with sign reversal (positive current) shown in Figure 4b were actually observed also for different charge occupation configurations and for both spin blockaded and non spin blockaded current triangles (Section 3, Supporting Information). In all cases, the position and the relative intensities of the four positive current peaks perfectly match position and intensity of the triple points measured at $V_{DS} \simeq 0$, as reported in Figure 4c.

In order to rationalize our results both at zero and finite V_{DS}, we adopt a semiclassical picture of radiation-matter interaction where MWs are treated classically while NW-DQDs are in quantum transport regime. Moreover, we assume that the MW field couples preferentially with one of the leads—for example, the drain—driving oscillations in its chemical potential. In this frame, we qualitatively explain the MW impact on the charge stability diagram at zero SD bias as the effect of a shaking of the addition energies in the lead, which broaden the region where tunneling is permitted along the filling direction, according to the schematic depicted in **Figure 5**a. This semiclassical picture also accounts for the impact of MWs at finite applied SD bias. To show this, we consider a total effective bias, V_{DS}^{tot}, which spans the range $V_{DS} - V_{AC} < V_{DS}^{tot} < V_{DS} + V_{AC}$, where V_{AC} is the amplitude of the MW perturbation (Figure 5b). All the bias configurations in this range may contribute to electron tunneling through the NW-DQD. The size of the current triangles is determined by the largest absolute value of the total bias. that is, $V_{DS}^{tot} = V_{DS} - V_{AC}$ (being $V_{DS} < 0$), corresponding to the configuration shown in Figure 5c. The opposite extreme of the bias range, where $V_{DS}^{tot} = V_{DS} + V_{AC}$, corresponds to the schematic depicted in Figure 5d). For $V_{AC} \geqslant |V_{DS}|$, a current sign reversal can be observed.

On the base of this model, we interpret the main results reported in Figure 4b, namely, the increased size of current triangles and the occurrence of current spots with sign reversal

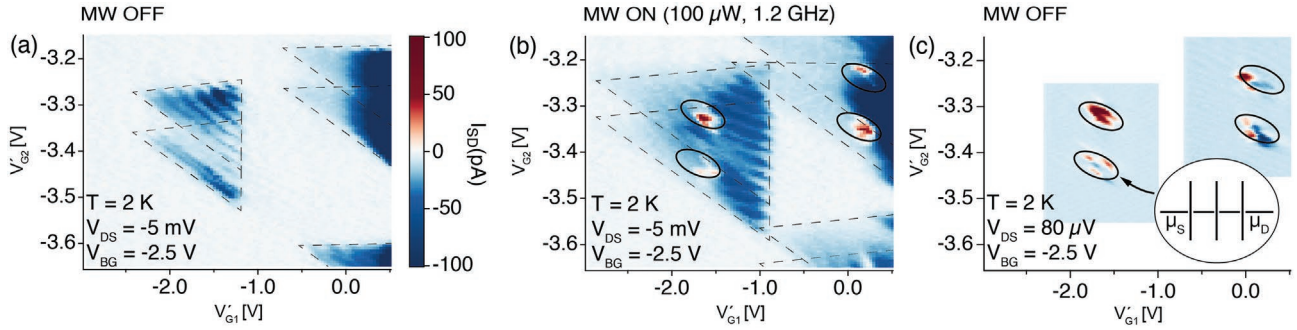

Figure 4. Current triangles measured at finite bias without MW excitation (a) and upon MW input power of 100 μW (b). Black dotted lines mark the edges of the current triangles. Black circles in (b) mark the onset of four current spots with sign reversal with respect to the full triangles. c) Current triple points measured at vanishing bias, marked with black circles. The locations of the black circles in panels (b) and (c) show an excellent match.

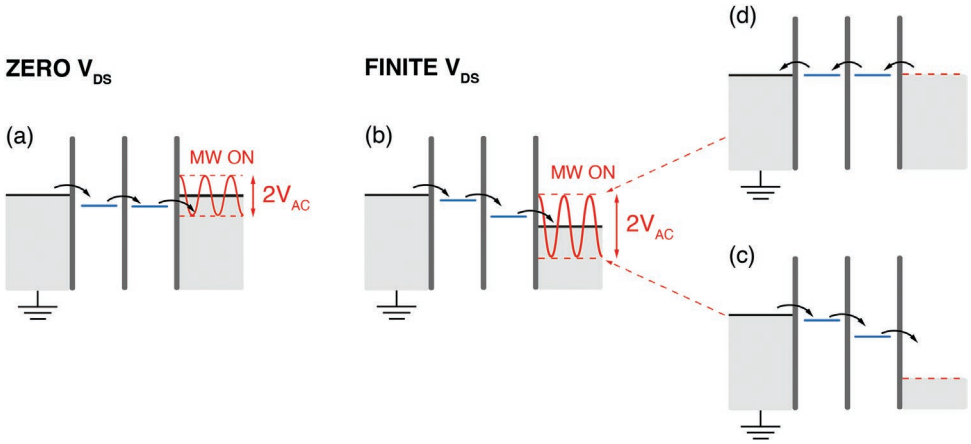

Figure 5. a) Schematic illustration of the model based on an effective AC bias (V_{AC}) used to rationalize the interaction of microwaves with NW-DQDs at vanishing-bias. V_{AC} is assumed to couple preferentially with the drain. b) Schematic illustration of the effective V_{AC} bias model used to rationalize the MW-DQD interaction at finite V_{DS}. The oscillating potential $V_{DS}^{tot} = V_{DS} \pm V_{AC}$ (red-colored in (b)) imposes a bias window for electron tunneling spanning from configuration (c) to (d). c) The effective AC oscillation brings the DQD to the maximum voltage bias configuration, d) the effective AC oscillation brings the DQD to the minimum (zero-) voltage bias configuration.

at triple points position. On the one hand, the triangle size increase is due to the DQD configuration depicted in Figure 5c. From the triangle size a $V_{DS}^{eff} = -10 \pm 1$ mV was extracted. Under the discussed model, $V_{DS}^{eff} = V_{DS}^{tot} = V_{DS} - V_{AC}$ where $V_{DS} < 0$. Since $V_{DS} = -5$ mV, we extract $V_{AC} = 5 \pm 1$ mV. On the other hand, the current spots with sign reversal originate from the DQD configuration shown in Figure 5(d). In this configuration, as an effect of the oscillating V_{AC}, the chemical potential of the source and drain electrodes are aligned, corresponding to vanishing positive bias V_{DS}^{tot}, thus generating the conditions for a current flow direction reversal. This scenario is in very good agreement with the V_{AC} values extracted above, since $V_{DS}^{tot} = V_{DS} + V_{AC} = 0 \pm 1$ mV. In this picture, the current inversion spot is enabled by the amplitude of V_{AC}, which in turn is determined by the impinging power, while it does not directly depend on the radiation frequency.

Strikingly, this framework provides an absolute reference—the applied bias voltage—for the evaluation of the local amplitude of the MW field, a physical quantity which is otherwise exceedingly difficult to measure, estimate or calculate. This can be achieved without the need for any calibration and resorting to the unique transport features of InAs/InP NW-DQD detectors. The self-calibration of InAs/InP NW-DQD MW detectors implies an assessment of the relationship between the effective V_{AC} and the photocurrent I_{ph}, which are measured exploiting two different device configurations. To this aim, we first extract the electrical impedence as $Z = V_{AC}/I_{ph}$. For applied MW field of 12 μW at 5 GHz, we estimate Z= 160 MΩ (see Section 5, Supporting Information). Then, we compare this value to the one calculated starting from the measured DQD resistance, R_{eq} and capacitance, C, obtained from the analysis of the conductive configurations in the current maps at zero and finite bias. In this case we found that Z is dominated by the resistive component R_{eq} which measures 65 MΩ (Section 5, Supporting Information). While the discrepancy between the two estimates of Z (factor ≈2.5) could be fixed by directly measuring the complex admittance of the device[39]; however, the two values are sufficiently similar to validate the relationship $V_{AC} = ZI_{ph}$. This allows us to estimate the dissipated power at the device, P_{diss}, as $P_{diss} = V_{AC} I_{ph}$, from which we calculated $P_{diss} = 1.5 \times 10^{-15}$ W (for V_{AC}=0.5 mV, I_{ph}=3 pA, P=12 μW, ν=5 GHz).

Finally, this bring us to fix the issue concerning the actual absorption of MW radiation in the NW cross-section. Indeed, the ratio between the dissipated and impinging powers, P_{diss}/P, provides a direct estimate of the total MW losses, accounting for both the MW power losses due to the antenna-detector coupling (quantified by L_{AD}, introduced in Chapter 2.3) and for the losses associated to non-unitary absorption in the NW cross-section, that we quantified by the parameter L_{CS}. Thus, we can write $P_{diss}/P = L_{CS} \times L_{AD}$, from which we estimate $L_{CS} = 3.6 \times 10^{-6}$. By accounting for L_{CS} in the renormalization of the MW power, we can further renormalize the values of the maximum R and η and minimum NEP, obtaining 2000 A W^{-1}, 0.04 and 10^{-16} W per $\sqrt{Hz}$, respectively: these values correspond to an optimal MW-detector coupling. These figures of merit can be compared with nanoscale quantum-confined semiconductor devices including noise detectors operated in the 10-80 GHz range[23,24] and DQD devices coupled to MW resonators.[16] For the former architecture, a quantum efficiency of 10^{-5} was computed by measuring the rates of competing relaxation mechanisms for photoexcited electrons. Our estimate of the quantum efficiency at the optimal coupling condition (4×10^{-2}) captures the intrinsic efficiency of the detection mechanism by taking into account the external power losses. In the latter architecture, the high efficiencies reported (6×10^{-2}) came at the cost of a quite complicated device architecture and an operating frequency locked at the resonator's one (f = 6.4 GHz).

3. Conclusions

Microwaves are efficiently detected by probing their impact on the transport properties of electrons tunneling across InAs/InP nanowire DQD-based devices. The nanodevices, equipped with source and drain electrodes and three independently biased gates, were exposed to microwave radiation (1–10 GHz,

0.1–100 μW) and the changes induced by the microwaves in the charge stability diagram at zero and finite source-drain bias were mapped as function of the MW intensity and frequency. The results at zero bias show that our devices act as power law MW detectors and allow us to extract lower thresholds for the figures of merit: responsivity R, quantum efficiency η and the NEP. The results at finite V_{DS} show current triangle magnification along filling and detuning directions together with the emergence of current spots with sign reversal. The experimental outcomes at both vanishing and finite bias are rationalized with a phenomenological model invoking an effective AC bias to account for the coupling between the microwaves and the NW-DQDs. Combining zero and finite-bias results with the model we envision that our devices are capable of microwave detection with unprecedented figures of merit $R \approx 2000$ A W^{-1}, $\eta \approx 0.04$ and $NEP \approx 10^{-16}\,\mathrm{W}/\sqrt{Hz}$. The present study demonstrates that NW-DQD-based devices allow us to measure the amplitude of the local MW field with an absolute reference—the equivalent source-drain bias—without requiring any calibration process. The peculiar transport features allowing for absolute MW detection, together with the high sensitivity and the nanometer-scale resolution, make InAs/InP NW DQDs a class of nanomaterials with the potentiality to act as game-changer for future MW detection platforms and applications.

4. Experimental Section

Nanomaterials Growth: InAs/InP nanowires were grown by metal-assisted chemical beam epitaxy, starting from an Au seed obtained by thermal dewetting on an InAs(111) substrate. NW diameters were found in the range 55–60 nm. Alternating Tert-Butyl-Arsine, Trimethyl-Indium and Tert-Butyl-Phosphine, three layers of InP (nominal thickness 5 nm) separated by two InAs sections (nominal thickness 20 nm and 23 nm) were grown inside the NW body. Further details can be found in ref. [30].

Device Fabrication: The grown nanowires were sonicated in isopropyl alcohol and then deposited by dropcasting on pre-patterned substrates with a 300 nm SiO_2 insulating layer on top of highly doped Si. Electron beam lithography was used to patter the devices, followed by O_2 plasma ashing, passivation in a NH_4S_x solution[40] and thermal evaporation of Cr (10 nm)/Au (100 nm). With the final liftoff the source, drain and side-gate contacts were defined.

Transport Measurements: The devices were characterised in a cryostat (temperatures of 2–8 K), wired with 16 filtered DC contacts and 2 RF lines (see also Section 8, Supporting Information).

Supporting Information

Supporting Information is available from the Wiley Online Library or from the author.

Acknowledgements

The authors thank Dr. Francesca Rossi for the TEM analysis of the nanowires. This research was funded by Italian MIUR, program PRIN 2017, project "Photonic Extreme Learning Machine" (PELM), protocol number 20177PSCKT, by the FET open project AndQC, H2020 Grant No. 828948 and the FET open project SUPERGALAX, Grant No. 863313.

Open access funding provided by Universita degli Studi di Modena e Reggio Emilia within the CRUI-CARE agreement.

Conflict of Interest

The authors declare no conflict of interest.

Data Availability Statement

The data that support the findings of this study are available from the corresponding author upon reasonable request.

Keywords

double quantum dots, InAs/InP nanowires, microwaves, nanoscale detectors

Received: October 28, 2022
Revised: December 28, 2022
Published online:

[1] B. M. Moloney, D. O'Loughlin, S. Abd Elwahab, M. J. Kerin, *Diagnostics* **2020**, *10*, 103.
[2] Z.-L. Xiang, S. Ashhab, J. Q. You, F. Nori, *Rev. Mod. Phys.* **2013**, *85*, 623.
[3] X. Gu, A. F. Kockum, A. Miranowicz, Y.-x. Liu, F. Nori, *Phys. Rep.* **2017**, *718–719*, 1.
[4] E. Vahapoglu, J. P. Slack-Smith, R. C. C. Leon, W. H. Lim, F. E. Hudson, T. Day, T. Tanttu, C. H. Yang, A. Laucht, A. S. Dzurak, J. J. Pla, *Sci. Adv.* **2021**, *7*, eabg9158.
[5] A. Blais, R.-S. Huang, A. Wallraff, S. M. Girvin, R. J. Schoelkopf, *Phys. Rev. A* **2004**, *69*, 062320.
[6] K. Grainge, B. Alachkar, S. Amy, D. Barbosa, M. Bommineni, P. Boven, R. Braddock, J. Davis, P. Diwakar, V. Francis, R. Gabrielczyk, R. Gamatham, S. Garrington, T. Gibbon, D. Gozzard, S. Gregory, Y. Guo, Y. Gupta, J. Hammond, D. Hindley, U. Horn, R. Hughes-Jones, M. Hussey, S. Lloyd, S. Mammen, S. Miteff, V. Mohile, J. Muller, S. Natarajan, J. Nicholls, et al., *Astron. Rep.* **2017**, *61*, 288.
[7] ADMX Collaboration, N. Du, N. Force, R. Khatiwada, E. Lentz, R. Ottens, L. J. Rosenberg, G. Rybka, G. Carosi, N. Woollett, D. Bowring, A. S. Chou, A. Sonnenschein, W. Wester, C. Boutan, N. S. Oblath, R. Bradley, E. J. Daw, A. V. Dixit, J. Clarke, S. R. O'Kelley, N. Crisosto, J. R. Gleason, S. Jois, P. Sikivie, I. Stern, N. S. Sullivan, D. B. Tanner, G. C. Hilton, *Phys. Rev. Lett.* **2018**, *120*, 151301.
[8] A. Ghirri, S. Cornia, M. Affronte, *Sensors* **2020**, *20*, 4010.
[9] F. Rossella, V. Piazza, M. Rocci, D. Ercolani, L. Sorba, F. Beltram, S. Roddaro, *Nano Lett.* **2016**, *16*, 5521.
[10] T. Takahashi, K. Kawaguchi, M. Sato, M. Suhara, N. Okamoto, *AIP Adv.* **2020**, *10*, 085218.
[11] E. Lind, *Semicond. Sci. Technol.* **2016**, *31*, 093005.
[12] M. Asgari, L. Viti, V. Zannier, L. Sorba, M. S. Vitiello, *Nanomaterials* **2021**, *11*, 3378.
[13] K. Peng, M. B. Johnston, *Appl. Phys. Rev.* **2021**, *8*, 041314.
[14] K. D. Petersson, L. W. McFaul, M. D. Schroer, M. Jung, J. M. Taylor, A. A. Houck, J. R. Petta, *Nature* **2012**, *490*, 380.
[15] S. Cornia, F. Rossella, V. Demontis, V. Zannier, F. Beltram, L. Sorba, M. Affronte, A. Ghirri, *Sci. Rep.* **2019**, *9*, 19523.
[16] W. Khan, P. P. Potts, S. Lehmann, C. Thelander, K. A. Dick, P. Samuelsson, V. F. Maisi, *Nat. Commun.* **2021**, *12*, 5130.
[17] A. Pfund, I. Shorubalko, R. Leturcq, K. Ensslin, *Appl. Phys. Lett.* **2006**, *89*, 252106.

[18] C. Fasth, A. Fuhrer, L. Samuelson, V. N. Golovach, D. Loss, *Phys. Rev. Lett.* **2007**, *98*, 266801.
[19] T. R. Hartke, Y.-Y. Liu, M. J. Gullans, J. R. Petta, *Phys. Rev. Lett.* **2018**, *120*, 097701.
[20] D. de Jong, C. G. Prosko, D. M. A. Waardenburg, L. Han, F. K. Malinowski, P. Krogstrup, L. P. Kouwenhoven, J. V. Koski, W. Pfaff, *Phys. Rev. Appl.* **2021**, *16*, 014007.
[21] Y.-Y. Liu, J. Stehlik, C. Eichler, M. J. Gullans, J. M. Taylor, J. R. Petta, *Science* **2015**, *347*, 285.
[22] Y.-Y. Liu, K. D. Petersson, J. Stehlik, J. M. Taylor, J. R. Petta, *Phys. Rev. Lett.* **2014**, *113*, 036801.
[23] S. Gustavsson, M. Studer, R. Leturcq, T. Ihn, K. Ensslin, D. C. Driscoll, A. C. Gossard, *Phys. Rev. Lett.* **2007**, *99*, 206804.
[24] R. Leturcq, S. Gustavsson, M. Studer, T. Ihn, K. Ensslin, D. Driscoll, A. Gossard, *Phys. E* **2008**, *40*, 1844.
[25] C. H. Wong, M. G. Vavilov, *Phys. Rev. A* **2017**, *95*, 012325.
[26] V. Zannier, F. Rossi, D. Ercolani, L. Sorba, *Nanotechnology* **2019**, *30*, 094003.
[27] L. Romeo, S. Roddaro, A. Pitanti, D. Ercolani, L. Sorba, F. Beltram, *Nano Lett.* **2012**, *12*, 4490.
[28] Z. S. Momtaz, S. Servino, V. Demontis, V. Zannier, D. Ercolani, F. Rossi, F. Rossella, L. Sorba, F. Beltram, S. Roddaro, *Nano Lett.* **2020**, *20*, 1693.
[29] F. S. Thomas, A. Baumgartner, L. Gubser, C. Jünger, G. Fülöp, M. Nilsson, F. Rossi, V. Zannier, L. Sorba, C. Schönenberger, *Nanotechnology* **2020**, *31*, 135003.
[30] F. Rossella, A. Bertoni, D. Ercolani, M. Rontani, L. Sorba, F. Beltram, S. Roddaro, *Nat. Nanotechnol.* **2014**, *9*, 997.
[31] D. Prete, P. A. Erdman, V. Demontis, V. Zannier, D. Ercolani, L. Sorba, F. Beltram, F. Rossella, F. Taddei, S. Roddaro, *Nano Lett.* **2019**, *19*, 3033.
[32] W. G. van der Wiel, S. De Franceschi, J. M. Elzerman, T. Fujisawa, S. Tarucha, L. P. Kouwenhoven, *Rev. Mod. Phys.* **2002**, *75*, 1.
[33] D. Barker, S. Lehmann, L. Namazi, M. Nilsson, C. Thelander, K. A. Dick, V. F. Maisi, *Appl. Phys. Lett.* **2019**, *114*, 183502.
[34] P. G. Datskos, N. V. Lavrik, in *Encyclopedia of Optical and Photonic Engineering*, 2nd edn., CRC Press, ISBN 978-1-351-24718-4, **2015**, pp. 1–9.
[35] L. P. Kouwenhoven, S. Jauhar, K. McCormick, D. Dixon, P. L. McEuen, Y. V. Nazarov, N. C. van der Vaart, C. T. Foxon, *Phys. Rev. B* **1994**, *50*, 2019.
[36] R. H. Blick, R. J. Haug, D. W. van der Weide, K. von Klitzing, K. Eberl, *Appl. Phys. Lett.* **1995**, *67*, 3924.
[37] H. Thierschmann, M. Henke, J. Knorr, L. Maier, C. Heyn, W. Hansen, H. Buhmann, L. W. Molenkamp, *New Journal of Physics* **2013**, *15*, 123010.
[38] S. Dorsch, A. Svilans, M. Josefsson, B. Goldozian, M. Kumar, C. Thelander, A. Wacker, A. Burke, *Nano Lett.* **2021**, *21*, 988.
[39] T. Frey, P. J. Leek, M. Beck, J. Faist, A. Wallraff, K. Ensslin, T. Ihn, M. Büttiker, *Phys. Rev. B* **2012**, *86*, 115303.
[40] D. B. Suyatin, C. Thelander, M. T. Björk, I. Maximov, L. Samuelson, *Nanotechnology* **2007**, *18*, 105307.